Chapter 3

Reconfigurable Microstrip Parasitic Antenna with Continuous Beam Scanning Capability in H-plane

3.1 Introduction

In this chapter, a reconfigurable microstrip Yagi antenna is proposed to realize continuous and improved beam scanning from -40° to 40° in the H-plane. It is observed that the 1-D beam steerable PRA designs reported in the literature achieves discrete beam switching [6, 46, 47, 49], small beam deflection angle [50, 51, 55–57], and limited beam steerable states. Moreover, in most of the microstrip Yagi antenna designs, continuous change in the effective electrical size of the parasitic element is not demonstrated. The proposed antenna is designed using a square-shaped driven patch and two hexagonal slotted tunable parasitic elements placed in the H-plane. Mutual coupling between the driven and tunable parasitic elements is controlled by changing the capacitance of varactor diodes loaded in the hexagonal slot. Relative lead and lag of current due to change in the effective electrical size of tunable parasitic patch causes phase distribution across the elements, resulting in continuous scanning of the main beam. Performance of the proposed antenna is simulated and measured in three operating modes, namely RD, DR, and broadside. In RD and DR mode, the main beam is continuously scanned from 14.4° to 40° and -14.4° to -40° respectively. The main beam is directed to 0° in the broadside mode with a gain of 3.36 dBi. This antenna achieves an overall -10 dB bandwidth from 2.43 to 2.47 GHz in all the

operating modes without any impedance matching network. Reflection and radiation performance of the fabricated antenna shows good agreement with the simulation results.

The remainder of this chapter is organized as follows: Section 3.2 describes the proposed antenna design and its working principle. The geometrical design and simulation results of the reconfigurable dual-band antenna are discussed. This section also presents the selection methodology of varactor diode along with its DC biasing and insertion loss characteristics. The simulated and measured results in the three operating modes are described in Section 3.3. Summary of the chapter is presented in Section 3.4.

3.2 Antenna Design and Working Principle

3.2.1 Antenna Configuration

Figure 3.1 shows the geometrical design of the proposed three-element antenna. The planar Yagi antenna is formed by combining the Yagi-Uda array and microstrip radiator technique. Main beam of the antenna can be steered in the elevation plane by using mutual coupling and the Yagi-Uda principle. In the conventional Yagi-Uda dipole array, currents are induced on the parasitic dipoles through space. However, in the microstrip Yagi antenna, the energy is coupled to the neighboring elements through space as well as surface waves. Beam steering capability is determined by the magnitude and phase of the induced current on parasitic elements. In the Yagi-Uda dipole array, the parasitic element is made reflector by increasing its length as compared to the driven element. Whereas director behavior is obtained by making parasitic element shorter than driven element. In the proposed PRA, reflector and director characteristics are obtained by continuously varying the effective electrical size of tunable parasitic elements as compared to the driven element size.

The proposed antenna consists of a coaxial-feed square-shaped driven patch and two tunable parasitic elements operating near resonance placed in the H-plane. This antenna is designed using FR4 substrate which has following properties: dielectric constant ϵ_r = 4.3, thickness h = 1.6 mm and loss tangent $\tan\delta$ = 0.02. Full-wave simulation of the antenna is performed using Ansys HFSS [33]. The driven and two tunable parasitic elements are placed on the same plane, which helps to design a low profile antenna structure. In the conventional microstrip Yagi antenna designs, size of the reflector and director elements is different as compared to the size of the driven element. In the proposed antenna, size of the tunable parasitic elements is the same as that of the driven element and is represented by L. The two tunable parasitic elements are represented as P1 and P2. Each tunable parasitic element consists of a hexagonal slot loaded with two varactor

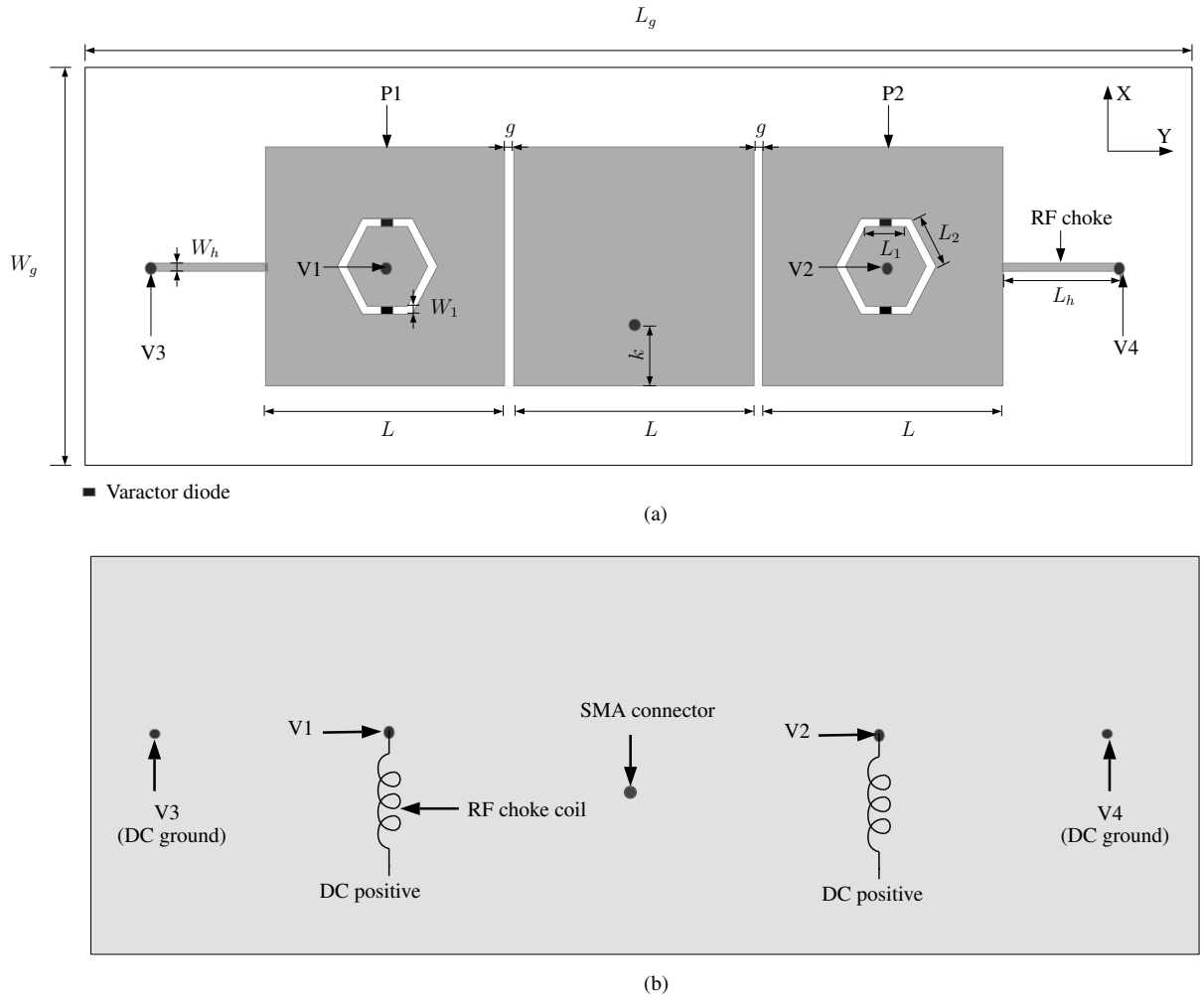

Figure 3.1. Geometrical design of the 1-D continuous beam scanning PRA (a) Front view and (b) Back view.

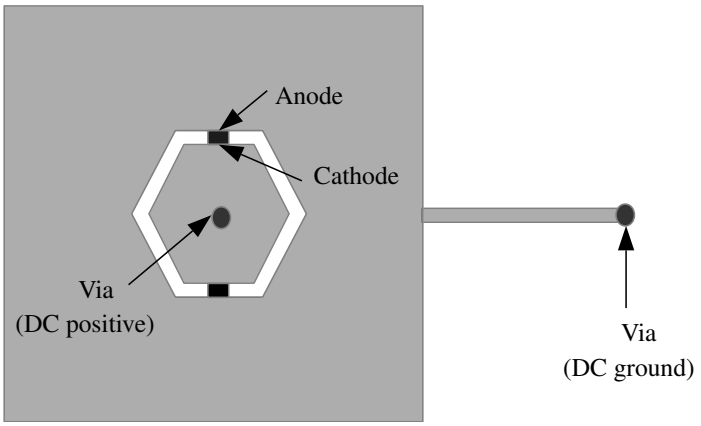

Figure 3.2. Enlarged view of the tunable parasitic element.

diodes, as shown in Figure 3.2. Inner and outer hexagonal element dimensions are represented by L_1 and L_2, respectively. The tunable parasitic element shows dual-band characteristics, and hence it can be resonated above and below the driven element center frequency of 2.45 GHz by changing the capacitance of varactor diode loaded in the hexagonal slot. The reconfigurable dual-band feature allows to continuously change the effective electrical size of the tunable parasitic element as compared to the driven element patch size. The driven and tunable parasitic elements are separated by a distance of g = 3 mm. This spacing is optimized to obtain good impedance matching and desired beam scanning. The coaxial-feed point distance from the patch edge is represented by k, and the feed point position is optimized to produce good impedance matching for all the capacitance values.

The proposed antenna is associated with a very simple DC biasing circuit. The driven element is a conventional square-shaped patch with no lumped components, and hence separate DC isolation circuit is not required to protect the VNA. DC voltage to the varactor diodes is applied using metallic vias placed between the top and bottom layers of the substrate. By using single via in each tunable parasitic element, both the varactor diodes are biased. Positive terminal of the DC supply is connected to the cathode of varactor diodes using vias V1 and V2 through a Coilcraft 4310LC-132KEB RF choke coil [148]. The coil is used to isolate the RF signal from the DC power supply, and it blocks high-frequency currents travelling to the DC power supply. This RF choke coil has flat bandwidth with high impedance up to 6 GHz. Anode terminal of the varactor diode is grounded using metallic vias V3 and V4, which are connected to a high impedance transmission line of length λ_g/4, where λ_g represents guided wavelength at 2.45 GHz. The length and width of the high impedance transmission line are represented by L_h and W_h, respectively. Optimized dimensions of the proposed antenna are summarized in Table 3.1.

Table 3.1. Optimized dimensions of the proposed 1-D continuous beam scanning PRA.

Parameter	Description	Size (mm)
L	Length of the driven and tunable parasitic element	28.9
L_1	Length of the inner hexagonal patch	5
L_2	Length of the outer hexagonal patch	5.5
W_1	Width of the hexagonal slot	0.5
g	Gap between the driven and tunable parasitic element	3
k	Length of the feed point from the patch edge	8.95
L_h	Length of the high impedance transmission line	16
W_h	Width of the high impedance transmission line	1.5
L_g	Length of the substrate	140
W_g	Width of the substrate	80

3.2.2 Reconfigurable Dual-band Antenna

Slot antennas are commonly used to achieve frequency agility since active or passive lumped components can be easily integrated [149–151]. Here, RA with dual-band characteristics is designed using a square-shaped patch and a hexagonal slot loaded with two varactor diodes. The geometrical design of the reconfigurable dual-band antenna is shown in Figure 3.3. In order to achieve dual-band characteristics, the varactor diodes are placed along the coaxial-feed. Hexagonal slot is selected since it provides two orthogonal slot locations along the feed to place the varactor diodes. The coaxial-feed square-shaped patch of length L is designed to operate at a frequency of f = 2.45 GHz. Initial size of the square-shaped patch can be determined by the following equation [152],

$$L = \frac{\lambda_0}{2\sqrt{\epsilon_r}} \tag{3.1}$$

where, L is length of the square-shaped patch, λ_0 is free space wavelength at an operating frequency of 2.45 GHz and ϵ_r is relative permitivity of the dielectric substrate. From this equation, length of the square-shaped patch is found to be 29.5 mm. This length is then optimized using HFSS to obtain best reflection characteristics at 2.45 GHz. Optimized dimensions of the reconfigurable dual-band antenna are as follows (in mm): L = 28.5, L_1 = 5, L_2 = 5.5, W_1 = 0.5, k = 8.75, L_g = 60 and W_g = 60.

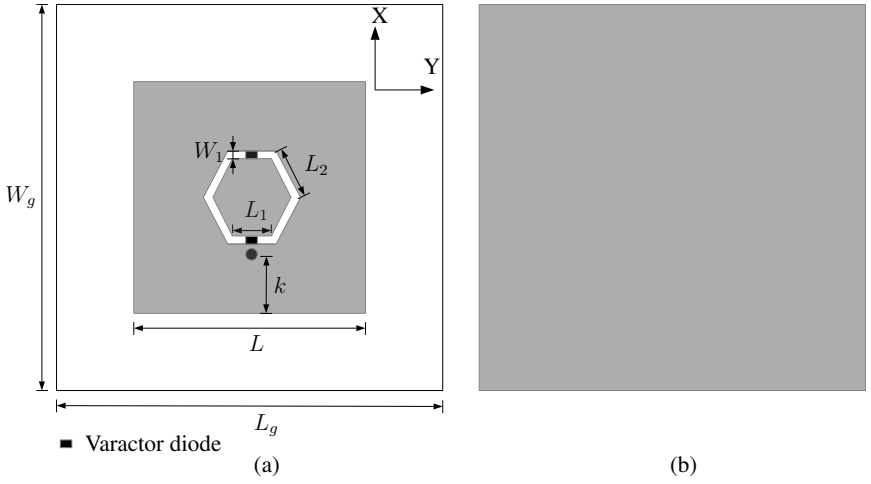

Figure 3.3. Geometrical design of the reconfigurable dual-band antenna (a) Front view and (b) Back view.

The reconfigurable dual-band antenna is simulated with different values of capacitance ranging from 0.5 to 7 pF. The antenna resonates at two frequencies f_1 = 2.30 GHz and f_2 = 4.50 GHz for 0.5 pF capacitance. Here, f_1 and f_2 represent lower and higher resonating frequency respectively. Figure 3.4 shows dual-band characteristics for 0.5 pF capacitance. Dual resonance is produced since the current on the antenna surface can travel in two directions. Figure 3.5 shows

the surface current distribution at the lower and higher resonating frequency, respectively. The lower resonance is produced when the current travels around the hexagonal slotted structure. The current also passes through the varactor diode, which decreases the effective electrical length of the antenna and thus producing higher resonance.

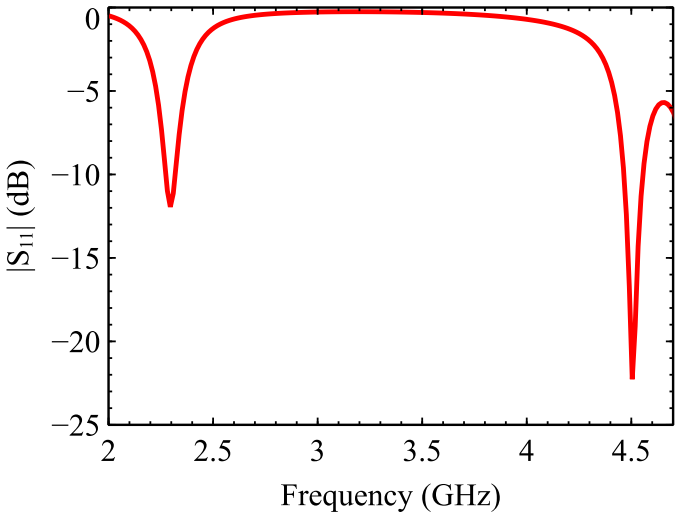

Figure 3.4. Dual-band characteristics for 0.5 pF capacitance.

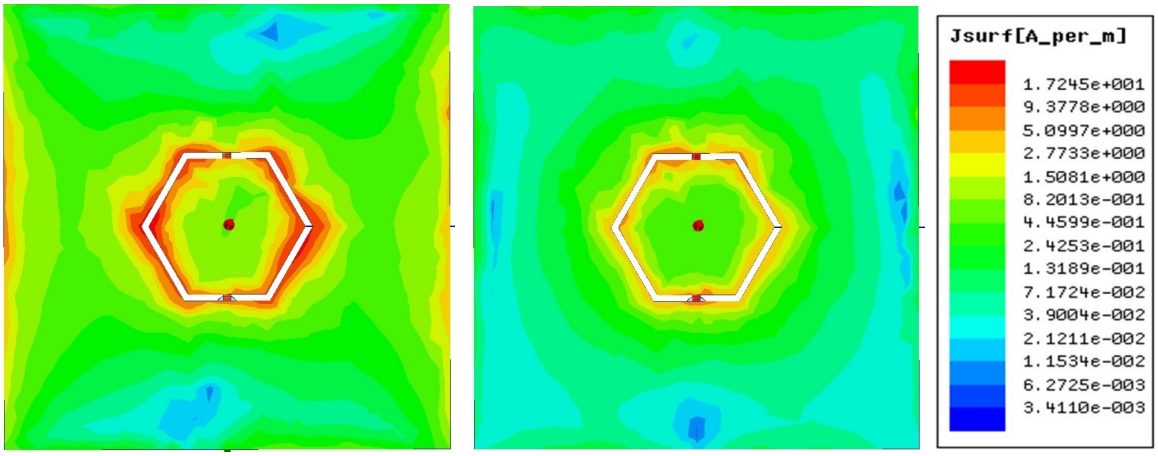

(A)

Figure 3.5. Surface current distribution for 0.5 pF capacitance (a) $f_1 = 2.30$ GHz and (b) $f_2 = 4.50$ GHz.

Table 3.2 summarizes simulated dual-band results obtained for the capacitance range from 0.5 to 7 pF. For the capacitance range from 0.5 to 0.9 pF, f_1 remains almost constant and f_2 starts decreasing from 4.50 to 3.54 GHz. For the capacitance range from 2 to 7 pF, f_1 decreases from 2.04 to 1.24 GHz, while f_2 starts approaching square patch center frequency $f = 2.45$ GHz. From Table 3.2, it can be observed that the variation in varactor diode capacitance from 0.5 to 7 pF changes the input impedance of the antenna. Therefore, the impedance matching is poor at both

resonant frequencies for the capacitance range from 1 to 2 pF. Nevertheless, the objective is to use this tunable antenna element to achieve continuous beam scanning characteristics. It is shown later in Section 3.2.5 that the frequencies that are close to the driven element center frequency of f = 2.45 GHz are alone important to realize continuous beam scanning. The proposed tunable antenna design shows good impedance matching at those frequencies.

Table 3.2. Dual-band characteristics for the capacitance range from 0.5 to 7 pF.

Capacitance (pF)	f_1 (GHz) $\|S_{11}\|$ (dB)	f_2 (GHz) $\|S_{11}\|$ (dB)
0.5	2.30 (−12)	4.50 (−23)
0.6	2.30 (−12)	4.20 (−21)
0.7	2.29 (−12)	3.95 (−16)
0.8	2.28 (−12)	3.71 (−12)
0.9	2.28 (−12)	3.54 (−9)
1	2.24 (−7)	3.29 (−4)
1.5	2.16 (−7)	-
2	2.04 (−9)	2.59 (−2)
3	1.79 (−29)	2.47 (−15)
4	1.59 (−13)	2.44 (−29)
5	1.43 (−9)	2.42 (−24)
6	1.32 (−6)	2.41 (−20)
7	1.24 (−5)	2.40 (−18)

Figure 3.6 shows the simulated radiation pattern at both the resonant frequencies for 0.5 pF capacitance. It can be seen that the antenna produces a broadside radiation pattern in both the principal planes. The simulated gain at the lower and higher resonating frequency is 2.36 dBi and 1.61 dBi, respectively. It is observed that the introduction of hexagonal slot causes cross-polarization for higher operating frequencies, which are obtained at lower capacitance values. The maximum cross-polarization observed within the 3-dB beamwidth range is −7.35 dB.

3.2.3 Dual-band Analysis with SMV 1233-079 Varactor Diode

For practical implementation of the proposed continuous beam scanning PRA, Skyworks SMV 1233-079 varactor diode is selected [153]. The Skyworks silicon hyperabrupt junction varactor diodes are designed for use in wireless systems up to 10 GHz. This varactor diode has a capacitance ranging from 0.84 to 5.08 pF with the corresponding reverse voltage varying from 15 to 0 V, as shown in Figure 3.7. The SMV 1233-079 varactor diode is selected since it has a low series resistance, and its capacitance tuning range is sufficient to achieve the required beam scanning. The equivalent circuit of the varactor diode can be represented by a series combination of C_j, R_s and L_p, where C_j is variable junction capacitance, R_s is series resistance and L_p is

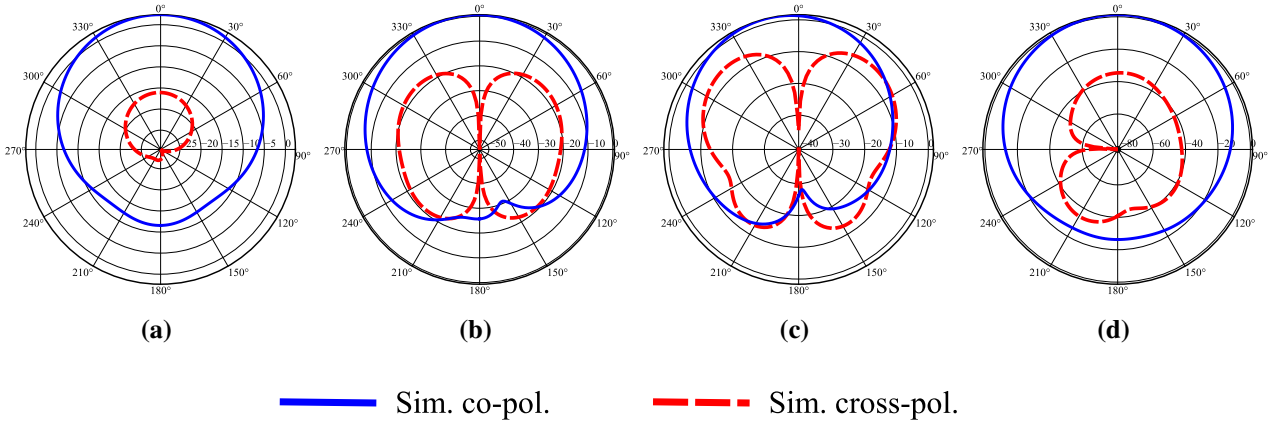

Figure 3.6. Normalized simulated radiation pattern at both the resonant frequencies for 0.5 pF capacitance (a) f_1 (E-plane), (b) f_1 (H-plane), (c) f_2 (E-plane) and (d) f_2 (H-plane).

parasitic inductance. Figure 3.8 depicts the equivalent circuit model of SMV1233-079 varactor diode. As per the Skyworks SMV 1233-079 datasheet, R_s is 1.2 Ω and L_p is 0.7 nH. A lumped series RLC circuit is used to accurately model the varactor diode in HFSS.

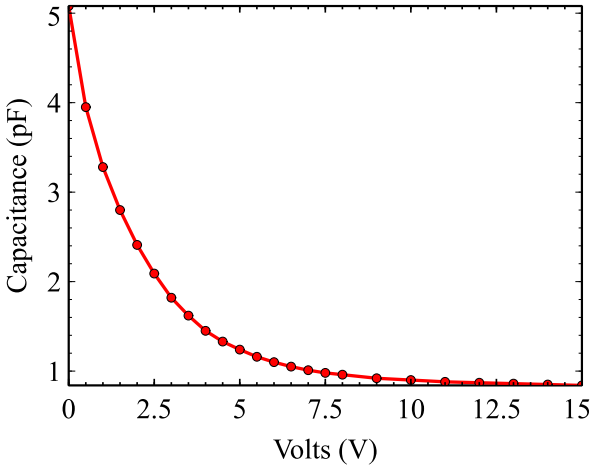

Figure 3.7. Capacitance value versus reverse biasing voltage of the Skyworks SMV 1233-079 varactor diode.

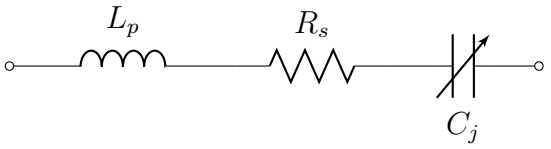

Figure 3.8. Equivalent circuit model of the Skyworks SMV 1233-079 varactor diode.

The performance of the reconfigurable dual-band antenna is analyzed in HFSS with actual capacitance values of SMV 1233-079 varactor diode. For the lower capacitance 0.84 pF the

antenna resonates at two frequencies f_1 = 2.28 GHz and f_2 = 3.65 GHz. For the capacitance range from 0.84 to 0.98 pF, f_1 is almost constant and f_2 starts decreasing from 3.65 to 3.42 GHz. As the capacitance increases from 1.82 to 5.08 pF, f_1 decreases from 2.10 to 1.43 GHz and f_2 starts approaching the square patch center frequency f. Figure 3.9 shows the dual-band response for 0.84 to 0.98 pF and 2.09 to 5.08 pF capacitance. Detailed simulation results for the capacitance range from 0.84 to 5.08 pF are presented in Table 3.3.

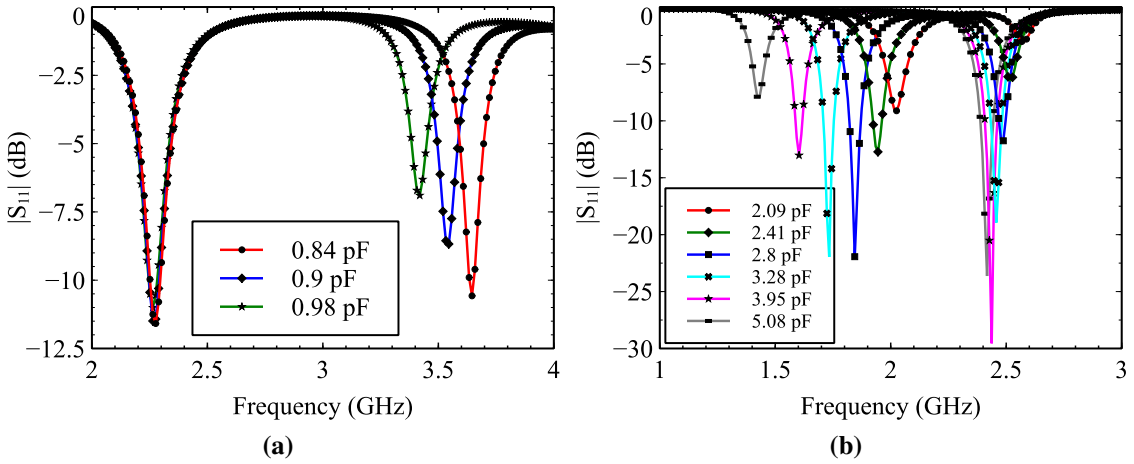

Figure 3.9. Dual-band characteristics for the capacitance range (a) 0.84 to 0.98 pF and (b) 2.09 to 5.08 pF.

Table 3.3. Dual-band characteristics for the capacitance range from 0.84 to 5.08 pF of SMV 1233-079 varactor diode.

Capacitance (pF)	f_1 (GHz) $\lvert S_{11}\rvert$ (dB)	f_2 (GHz) $\lvert S_{11}\rvert$ (dB)
0.84	2.28 (−11.59)	3.65 (−10.57)
0.9	2.26 (−11.49)	3.55 (−8.55)
0.98	2.26 (−11.00)	3.42 (−6.90)
1.82	2.10 (−8.49)	2.72 (−0.46)
2.09	2.02 (−9.11)	2.57 (−3.02)
2.41	1.95 (−12.72)	2.52 (−6.49)
2.8	1.85 (−21.93)	2.48 (−11.75)
3.28	1.73 (−21.96)	2.46 (−18.94)
3.95	1.60 (−13.02)	2.44 (−29.55)
5.08	1.43 (−7.88)	2.42 (−23.63)

The simulated radiation pattern for 0.84 pF and 5.08 pF capacitance is shown in Figure 3.10 and Figure 3.11, respectively. The antenna radiates in broadside direction since both the resonances are produced due to TM_{10} mode. The effect of hexagonal slot on the cross-polarization level is analyzed for the capacitance values from 0.84 to 5.08 pF, at both the operating bands. Maximum cross-polarized level of −17.53 dB is observed at 0.84 pF capacitance for the higher operating frequency of f_2 = 3.65 GHz. At all other capacitance values, the cross-polarization is found to be

below -18.33 dB. The proposed tunable antenna design achieves lower cross-polarization at the frequencies which are closer to driven element center frequency f = 2.45 GHz. The maximum cross-polarization level observed within the 3-dB beamwidth for the capacitance range from 0.84 to 5.08 pF is summarized in Table 3.4.

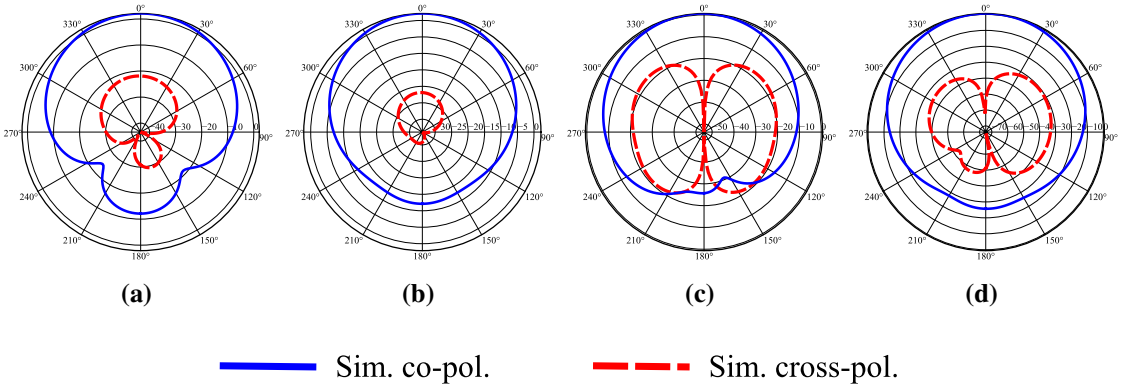

Figure 3.10. Normalized simulated radiation pattern at both the resonant frequencies for 0.84 pF capacitance (a) f_1 (E-plane), (b) f_1 (H-plane), (c) f_2 (E-plane) and (d) f_2 (H-plane).

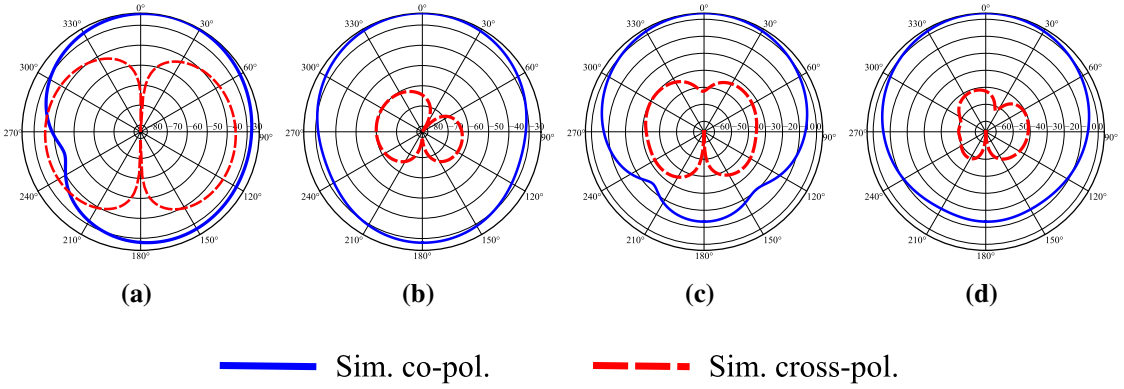

Figure 3.11. Normalized simulated radiation pattern at both the resonant frequencies for 5.08 pF capacitance (a) f_1 (E-plane), (b) f_1 (H-plane), (c) f_2 (E-plane) and (d) f_2 (H-plane).

3.2.4 Insertion Loss of Varactor Diode

To analyze insertion loss characteristics of SMV 1233-079 varactor diode a simple microstrip transmission line of characteristic impedance 50 Ω is designed and simulated in HFSS using FR4 substrate with following properties: ϵ_r = 4.3, $\tan\delta$ = 0.02 and h = 1.6 mm. The varactor diode is placed in the center of 50 Ω transmission line, as shown in Figure 3.12. Geometrical dimensions of the transmission line are as follows (in mm): L = 8.22 , L_1 = 0.5, W_1 = 3.12, L_g = 16.94 and W_g

Table 3.4. Maximum cross-polarization level within the 3-dB beamwidth at both the operating frequencies in E-plane and H-plane for the capacitance range 0.84 to 5.08 pF.

Capacitance (pF)	Cross-polar. (dB) f_1 (E-plane)	Cross-polar. (dB) f_1 (H-plane)	Cross-polar. (dB) f_2 (E-plane)	Cross-polar. (dB) f_2 (H-plane)
0.84	−23.98	−23.93	−17.53	−31.39
0.9	−21.38	−21.40	−18.62	−35.32
1.82	−36.05	−50.98	−18.33	−37.00
2.09	−33.83	−46.33	−24.21	−34.82
2.41	−32.12	−46.63	−27.92	−38.00
2.8	−27.20	−41.32	−29.88	−41.71
3.28	−24.80	−41.40	−33.05	−38.73
3.95	−19.00	−40.12	−35.31	−43.30
5.08	−18.66	−36.07	−33.77	−44.09

= 16.94. Capacitance of the varactor diode is varied from 0.84 to 5.08 pF. Figure 3.13(a) shows the simulated S-parameter response for 0.84 and 5.08 pF capacitance. Insertion loss of the varactor diode is found to be in the range of −0.45 to −1.77 dB at 2.45 GHz. From Figure 3.13(b), it can be observed that minimum insertion loss is obtained at the higher capacitance values.

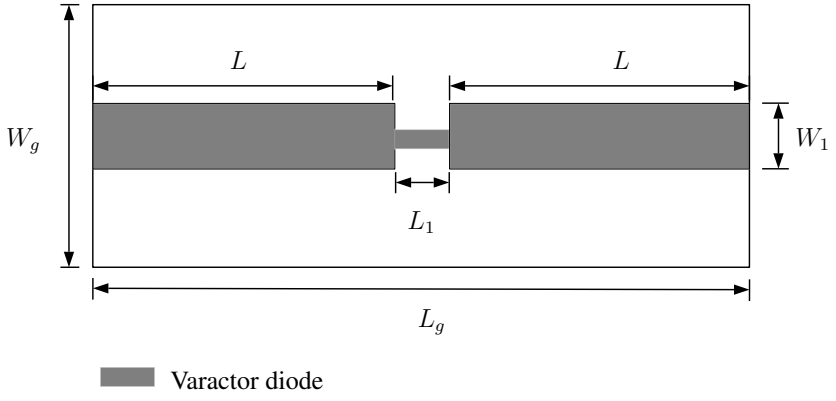

Figure 3.12. Geometrical model of 50 Ω microstrip transmission line loaded with varactor diode.

3.2.5 Working Principle

A Yagi-Uda principle and tunable parasitic patch size method is used to realize continuous beam scanning. The mutual coupling between the driven and tunable parasitic elements is controlled by varying the capacitance of varactor diodes. It is observed that the mutual coupling is strong when the size of a driven element is close to the effective electrical size of the tunable parasitic element. For 0.84 pF capacitance, the antenna resonates at two frequencies f_1 = 2.28 GHz and f_2 = 3.65 GHz. As $f_1 < f$, the effective electrical size of the tunable parasitic element is larger than the driven element. Thus, according to the Yagi-Uda principle, the tunable parasitic

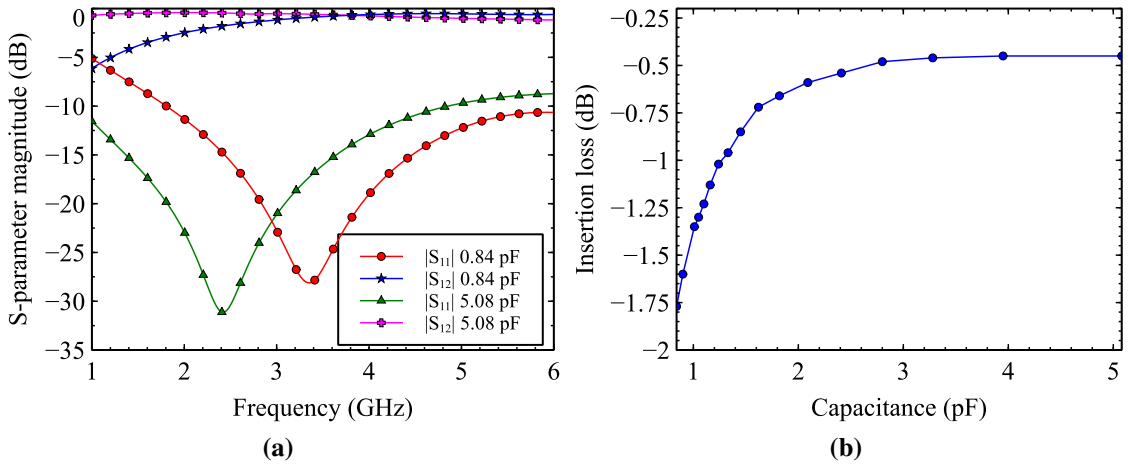

Figure 3.13. (a) Simulated S-parameter response of the SMV 1233-079 varactor diode for capacitance 0.84 pF and 5.08 pF and (b) Insertion loss characteristics for the capacitance range from 0.84 to 5.08 pF.

element shows inductive behavior and can be used as a reflector. There is no effect of f_2 on the radiation characteristics since $f_2 >> f$. As capacitance increases from 1.82 to 5.08 pF, f_1 starts decreasing, and thus the effective electrical size of the tunable parasitic element becomes very large as compared to the driven element. In this case, the mutual coupling between the antenna elements is very weak. However, f_2 starts decreasing and approaches the driven element center frequency f = 2.45 GHz. Hence, the size of tunable parasitic element becomes smaller than the driven element, and it can be used as a director. Thus, by varying the capacitance of varactor diodes, the tunable parasitic element can be used as a reflector, director, or neutral element. It can be concluded that at lower capacitance, the antenna shows reflector characteristics and at higher capacitance director characteristics. Table 3.5 shows capacitance values of the tunable parasitic elements P1 and P2 used in the three operating modes RD, broadside, and DR.

Table 3.5. Tunable Parasitic patch P1 and P2 capacitance values used in the three operating modes.

Operating Mode	P1 capacitance (pF)	P2 capacitance (pF)
RD	0.84	1.62 - 5.08
Broadside	1.82	1.82
DR	1.62 - 5.08	0.84

3.2.6 Parametric Analysis

In the microstrip Yagi antenna, important design parameters are the distance between the radiating elements and the size of the parasitic element. Parametric analysis is performed using HFSS

to investigate the effect of these parameters on antennas reflection and radiation characteristics. Detailed simulation results are presented in this section.

3.2.6.1 Effect of Distance between the Driven and Parasitic Element

Figure 3.14 shows the two-element microstrip Yagi antenna configuration utilized to analyze the effect of distance between the driven and parasitic element. Dimensions of the antenna are as follows (in mm): L = 28.9, k = 8.95, L_g = 100 and W_g = 60. This design consists of a driven element and one parasitic element placed in the H-plane. Size of the driven and parasitic element is represented by L. The antenna radiates with maximum steered angle, when both the elements are of the same size. Distance between the driven and parasitic element is varied from 1 mm to 5 mm.

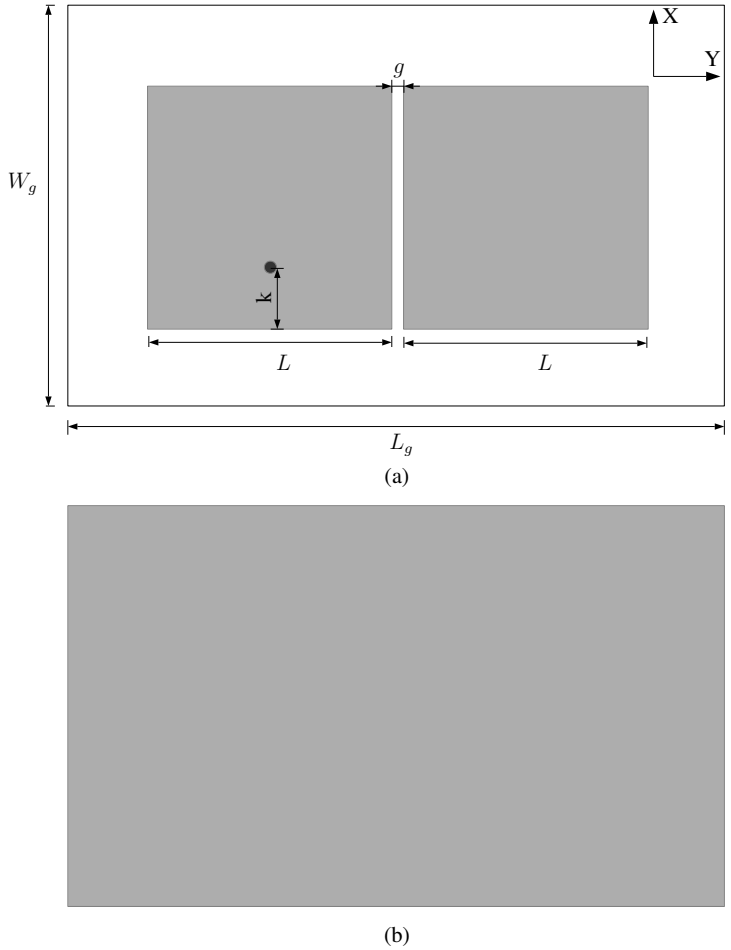

Figure 3.14. Geometrical design of the two-element microstrip Yagi antenna (a) Front view and (b) Back view.

Figure 3.15(a) presents simulated S-parameter characteristics, and it can be observed that for the spacing of 1 mm and 2 mm, the operating frequency of the antenna is shifted to 2.49 GHz and 2.47

GHz respectively. Distance between the antenna elements strongly affects impedance matching, and it is very difficult to obtain good matching at 2.45 GHz for the spacing less than 3 mm. For smaller spacing, coupling strength between the driven and parasitic element is maximum, as shown in Figure 3.15(b). For 3 mm spacing, the antenna shows good impedance matching at 2.45 GHz with an overall -10 impedance bandwidth from 2.42 to 2.48 GHz. Figure 3.16 shows the effect of distance between the driven and parasitic element on beam scanning characteristics. For 3 mm spacing, main beam of the antenna is directed to 28° with a gain of 2.33 dBi. For 4 mm and 5 mm spacing, the antenna shows good impedance matching at 2.45 GHz. However, the gain of the antenna in beam steered direction decreases, and SLL increases. From this analysis, it can be concluded that spacing between the driven and tunable parasitic elements is an important factor, which affects the impedance matching and radiation characteristics of the microstrip Yagi antenna. In the microstrip Yagi antenna configuration, the direction of the main beam is determined by the amplitude and phase of the induced current on the parasitic elements. The gap between the antenna elements affects the direction of main beam since the amplitude and phase of the mutually coupled field changes with the distance. Therefore, in the proposed antenna design, to obtain the best impedance matching, a large main beam angle and low SLL distance between the driven and parasitic elements is fixed to 3 mm.

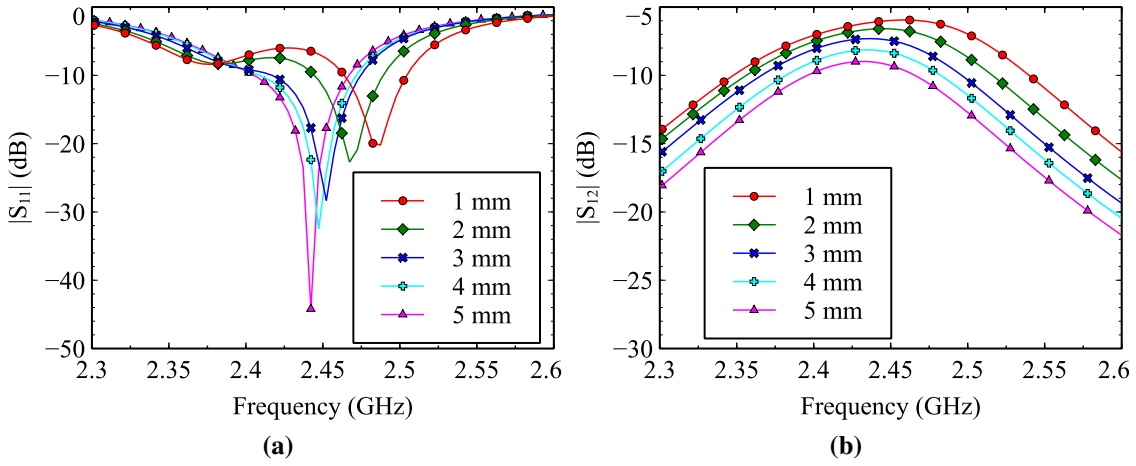

Figure 3.15. Effect of distance between the driven and parasitic element on (a) Reflection characteristics and (b) Mutual Coupling.

3.2.6.2 Effect of Parasitic Patch Size

The effect of size of the parasitic element on antennas reflection and radiation characteristics is analyzed by placing a parasitic element in the H-plane at a distance of 3 mm. Here, the size of the parasitic element is varied from 20 mm to 41 mm and size of the driven element is fixed

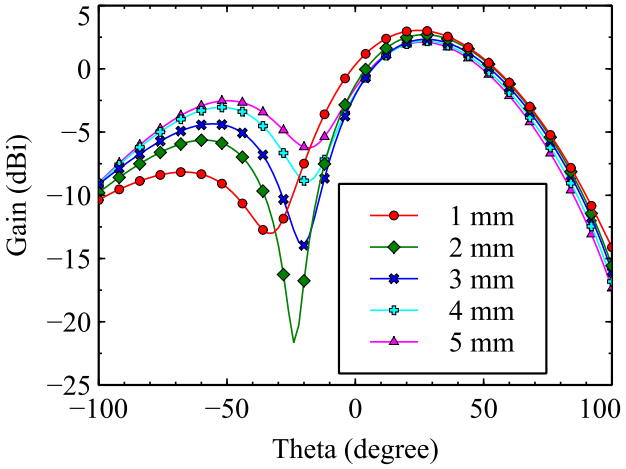

Figure 3.16. Effect of distance between the driven and parasitic element on radiation characteristics.

at 28.9 mm. From Figure 3.17, it can be observed that the main of the antenna is steered from -22° to 30°, as size of the parasitic element, is physically varied from 21 mm to 41 mm. For the size of 20 mm and 22 mm, the antenna radiates in broadside direction with a gain of 3.85 dBi. Mutual coupling between the driven and parasitic element is very weak, and the overall radiation pattern is nearly the same as that of the square-shaped driven element. As the size of the parasitic element is gradually varied from 20 mm to 28.9 mm, mutual coupling increases, and the main beam of the antenna is steered from 0° to 30° with a gain variation from 3.85 to 2.39 dBi. For the physical size of 28.9 mm, the antenna shows the best director characteristics, and the induced currents on the parasitic elements are maximum. Main beam of the antenna is steered to 30° with an SLL of -9.3 dB. As the physical size increased more than 28.9 mm, the antenna starts directing its beam in $-\theta$ direction. The main beam of the antenna is steered from -12° to -22°, as size of the parasitic element is varied from 30 mm to 41 mm. This antenna configuration shows the best reflector characteristics for the physical size of 41 mm, and the main beam of the antenna is directed to -22° with a gain of 3.21 dBi. In conclusion, by physically changing the size of the parasitic element from 20 mm to 41 mm, the main beam of the antenna is steered from -22° to 30°. However, it is not practically feasible to change the size of the parasitic element to realize beam steering. To achieve electronic beam steering, size of the parasitic element should be continuously changed as compared to size of the driven element. A reconfigurable dual-band antenna can be used to change the effective electrical size of parasitic element as compared to the driven element size by resonating it above and below the driven element center frequency of 2.45 GHz.

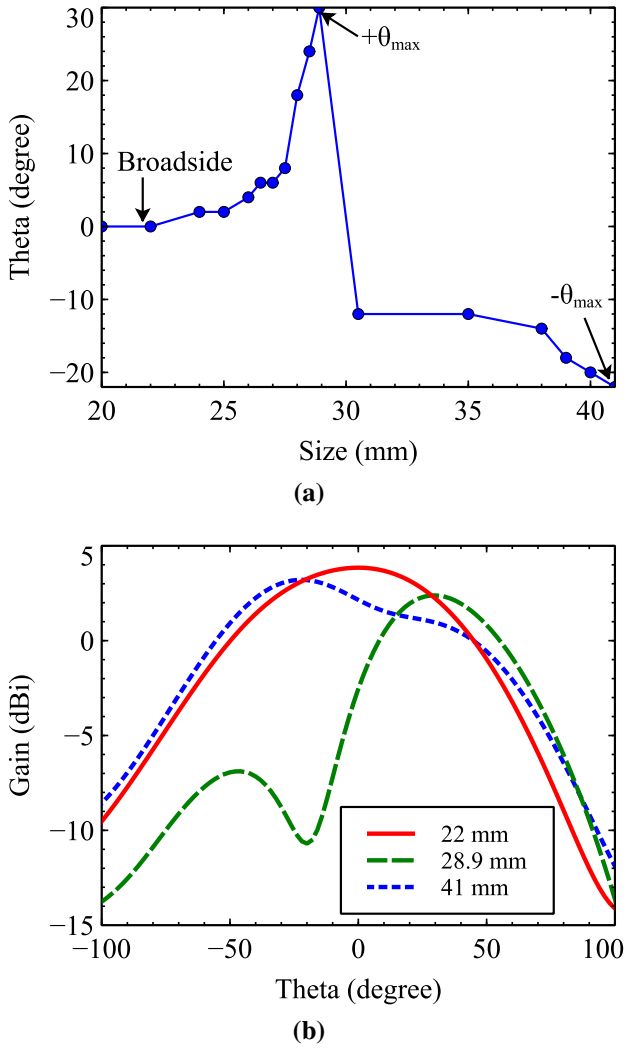

Figure 3.17. Effect of size of the parasitic element on radiation characteristics.

3.2.6.3 Effect of Tunable Parasitic Element

Figure 3.18 shows design of the two-element microstrip Yagi antenna consisting of driven element and one tunable parasitic element placed in the H-plane at a distance of 3 mm. Optimized dimensions of the antenna are as follows (in mm): L = 28.9, L_1 = 5, L_2 = 5.5, W_1 = 0.5 k = 8.95, g = 3, L_g = 100 and W_g = 60.

The effect of tunable parasitic element on reflection and radiation characteristics is analyzed by changing the capacitance of varactor diode from 0.84 to 5.08 pF. Figure 3.19 presents simulated radiation characteristics for the capacitance range from 0.84 to 5.08 pF. This antenna configuration shows good impedance matching for all the capacitance values with an overall -10 dB bandwidth from 2.42 to 2.47 GHz, as shown in Figure 3.20. Main beam of the antenna is continuously scanned from $-14°$ to 28°, as capacitance increases from 0.84 to 5.08 pF. The main beam is steered in $-\theta$ direction for the capacitance range 0.84 to 1.62 pF. It is observed that the best reflector

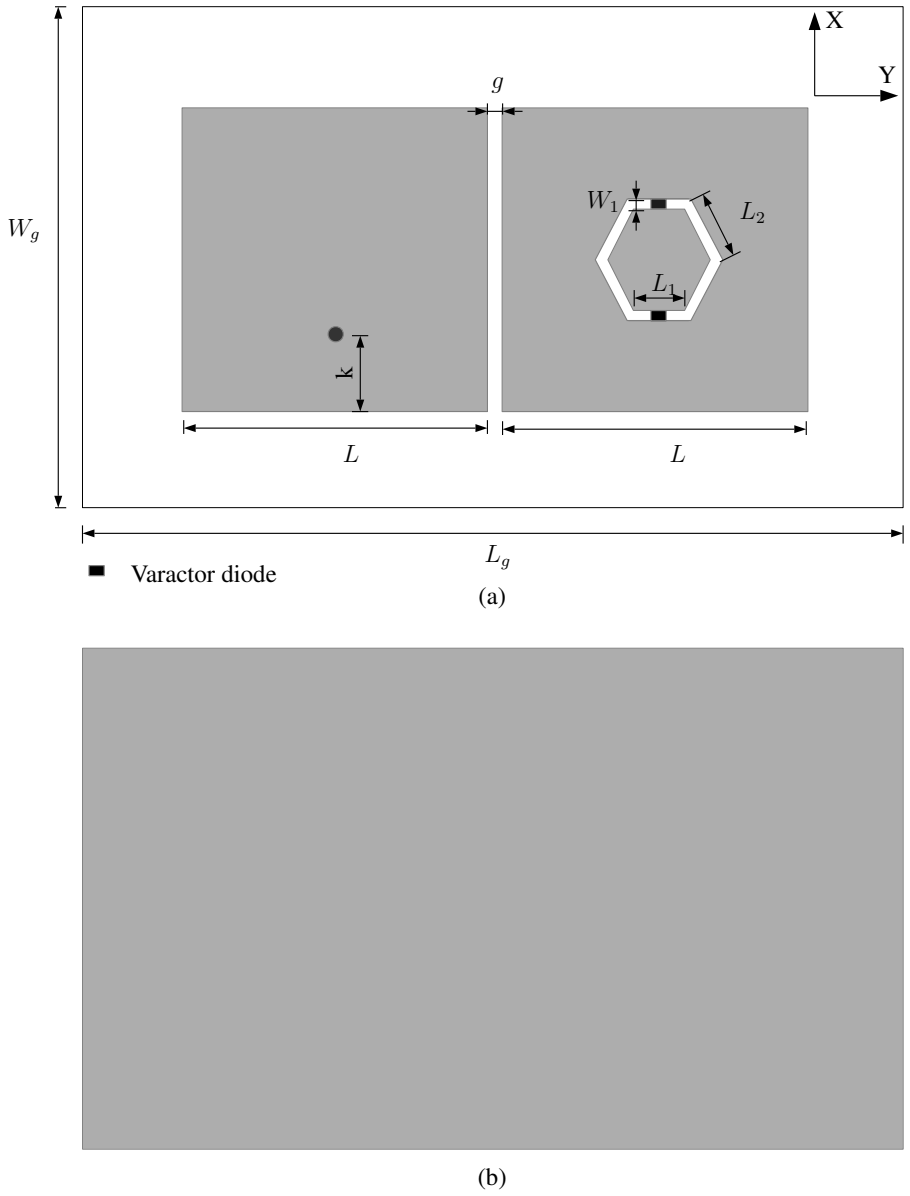

Figure 3.18. Geometrical design of the two-element microstrip Yagi antenna consisting of driven element and one tunable parasitic element (a) Front view and (b) Back view.

characteristics are obtained at 0.84 pF, which is the lower capacitance value of the SMV 1233-079 varactor diode. The capacitance range from 2.09 to 5.08 pF can be used to achieve director characteristics. For 1.82 pF capacitance, the antenna radiates in broadside direction with simulated gain and radiation efficiency of 3.47 dBi and 43%, respectively. For the higher capacitance range, the antenna radiates with a large tilted beam, but the gain and radiation efficiency decreases. The overall simulated gain and radiation efficiency is found to be in the range of 0.86 to 3.98 dBi and 23% to 44%, respectively. It is also noted that when the antenna radiates with maximum steered angle SLL starts increasing in the opposite direction of the main beam. The maximum SLL obtained at 5.08 pF is -1.75 dB. Simulated cross-polarization level within the 3-dB beamwidth

range is found to be less than −17.24 dB. This analysis leads to the conclusion that the main beam of the two-element microstrip Yagi antenna can be continuously scanned in the H-plane from −14° to 28° by changing the capacitance of varactor diode from 0.84 to 5.08 pF. However, with this configuration, asymmetrical beam scanning is obtained with high SLL.

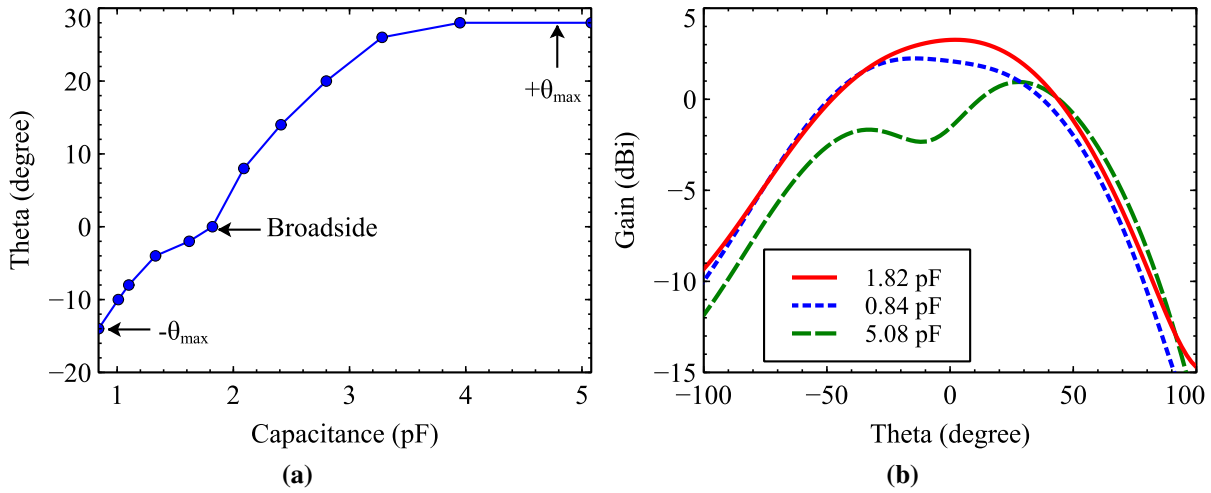

Figure 3.19. Effect of one tunable parasitic element placed in the H-plane on antennas radiation characteristics.

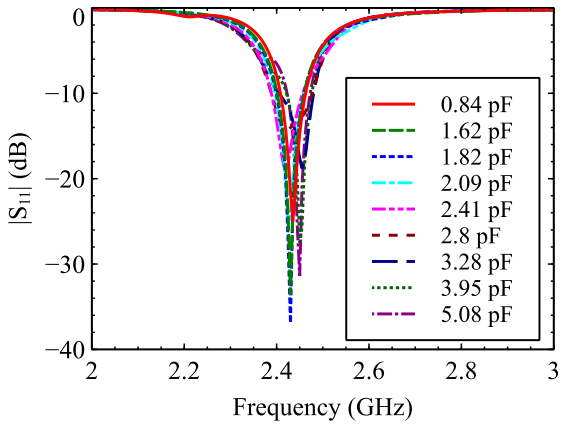

Figure 3.20. Simulated reflection characteristics of the microstrip Yagi antenna consisting of driven element and one tunable parasitic element.

3.2.6.4 Calculation of Current Ratios in Reflector-Director (RD), Director-Reflector (DR), and Broadside Mode

The effect of varactor diode capacitance on the mutual coupling is presented in this section. The current ratios are evaluated from the full-wave simulated three-port Z parameters and boundary conditions imposed by the variable reactive loads [50]. The relation between the voltages and

currents can be represented in terms of the Z matrix as,

$$\begin{bmatrix} V_1 \\ V_2 \\ V_3 \end{bmatrix} = \begin{bmatrix} Z_{11} & Z_{12} & Z_{13} \\ Z_{21} & Z_{22} & Z_{23} \\ Z_{31} & Z_{32} & Z_{33} \end{bmatrix} \begin{bmatrix} I_1 \\ I_2 \\ I_3 \end{bmatrix} \tag{3.2}$$

where, Z_{11}, Z_{22} and Z_{33} represents self impedances. Z_{12}, Z_{13}, Z_{21}, Z_{23}, Z_{31} and Z_{32} represents mutual impedances. The currents on the driven and tunable parasitic elements P1 and P2 are represented as I_1, I_2 and I_3. The values of self and mutual impedances are obtained from HFSS. The boundary conditions on the two ports are defined as,

$$Z_{C2} = 1/jwC_2, Z_{C3} = 1/jwC_3 \tag{3.3}$$

$$V_2 = -Z_{C2}I_2, V_3 = -Z_{C3}I_3 \tag{3.4}$$

where, C_2 and C_3 are the respective capacitance values on the tunable parasitic elements P1 and P2. The current ratios are evaluated by using (3.3) and (3.4) in (3.2).

$$\begin{bmatrix} Z_{22} + Z_{C2} & Z_{23} \\ Z_{32} & Z_{33} + Z_{C3} \end{bmatrix} = \begin{bmatrix} I_2/I_1 \\ I_3/I_1 \end{bmatrix} \begin{bmatrix} -Z_{21} \\ -Z_{31} \end{bmatrix} \tag{3.5}$$

$$\begin{bmatrix} I_2/I_1 \\ I_3/I_1 \end{bmatrix} = \begin{bmatrix} Z_{22} + Z_{C2} & Z_{23} \\ Z_{32} & Z_{33} + Z_{C3} \end{bmatrix}^{-1} \begin{bmatrix} -Z_{21} \\ -Z_{31} \end{bmatrix} \tag{3.6}$$

$$\frac{I_2}{I_1} = \frac{Z_{21}(-Z_{33} - Z_{C3}) + Z_{31}Z_{23}}{(Z_{22} + Z_{C2})(Z_{33} + Z_{C3}) - Z_{23}Z_{32}} \tag{3.7}$$

$$\frac{I_3}{I_1} = \frac{Z_{31}(-Z_{22} - Z_{C2}) + Z_{21}Z_{32}}{(Z_{22} + Z_{C2})(Z_{33} + Z_{C3}) - Z_{23}Z_{32}} \tag{3.8}$$

$|I_2/I_1|$ and $|I_3/I_1|$ gives the coupling strength between the driven element and tunable parasitic elements P1 and P2 respectively. In the RD mode, $|I_2/I_1|$ is almost constant, since the P1 parasitic capacitance is fixed at 0.84 pF. The coupling between the driven element and P2 starts increasing as capacitance increases from 2.41 to 5.08 pF. At 5.08 pF, $|I_3/I_1|$ is maximum, and strong currents are induced on the tunable parasitic element P2. In the DR mode, $|I_2/I_1|$ shows variations and $|I_3/I_1|$ is nearly constant. The current ratio between the antenna elements is small in the broadside mode, since the overall radiation is dominated by the driven element. Table 3.6 shows the current ratio values for the three operating modes RD, DR and broadside.

Table 3.6. Current ratio calculations in RD, DR and broadside mode.

Capacitance (pF)	RD Mode		DR Mode		Broadside Mode	
	$\lvert I_2/I_1\rvert$	$\lvert I_3/I_1\rvert$	$\lvert I_2/I_1\rvert$	$\lvert I_3/I_1\rvert$	$\lvert I_2/I_1\rvert$	$\lvert I_3/I_1\rvert$
1.62	0.12	0.11	0.10	0.12	-	-
1.82	0.12	0.07	0.07	0.12	0.06	0.06
2.09	0.11	0.07	0.07	0.11	-	-
2.41	0.10	0.18	0.18	0.11	-	-
2.8	0.09	0.31	0.33	0.10	-	-
3.28	0.09	0.46	0.46	0.09	-	-
3.95	0.10	0.56	0.56	0.10	-	-
5.08	0.10	0.65	0.66	0.10	-	-

3.3 Results and Discussion

In the previous Section 3.2, it has been shown that the main beam of the antenna is continuously scanned from -14° to 28° for a square-shape driven element with one tunable parasitic element, as the capacitance is varied from 0.84 to 5.08 pF. However, it is found that the reflector and director properties of the tunable parasitic elements can be used to achieve symmetrical and increased beam scanning with low SLL. The fabricated structure of the proposed antenna is shown in Figure 3.21(a). The magnified view of the tunable parasitic element is depicted in Figure 3.21(b). Performance of the proposed antenna is tested and verified in three operating modes RD, broadside, and DR. Reverse voltage to the varactor diodes is applied using Keithleys programmable DC power supply and Coilcrafts RF choke coil. Figure 3.21(c) shows a back view of the antenna. Measurements are performed by using Keysight E5063A VNA, as depicted in Figure 3.21(d). In the proposed three-element parasitic antenna design, the driven element is a conventional square-shaped patch with no slots, which helps to minimize the cross-polarization level. The measured overall cross-polarization level is found to be below -18.04 dB, -17.20 dB, and -20.54 dB in the RD, DR, and broadside mode respectively.

3.3.1 Reflector-Director (RD) Mode

The tunable parasitic element shows strong reflector characteristics at 0.84 pF. Therefore, in this mode, P1 capacitance is fixed at 0.84 pF. The P2 capacitance is increased from 1.62 to 5.08 pF. Reflection characteristics plotted in Figure 3.22 shows that the antenna maintains good impedance characteristics for all the capacitance values with overall measured bandwidth from 2.43 to 2.48 GHz.

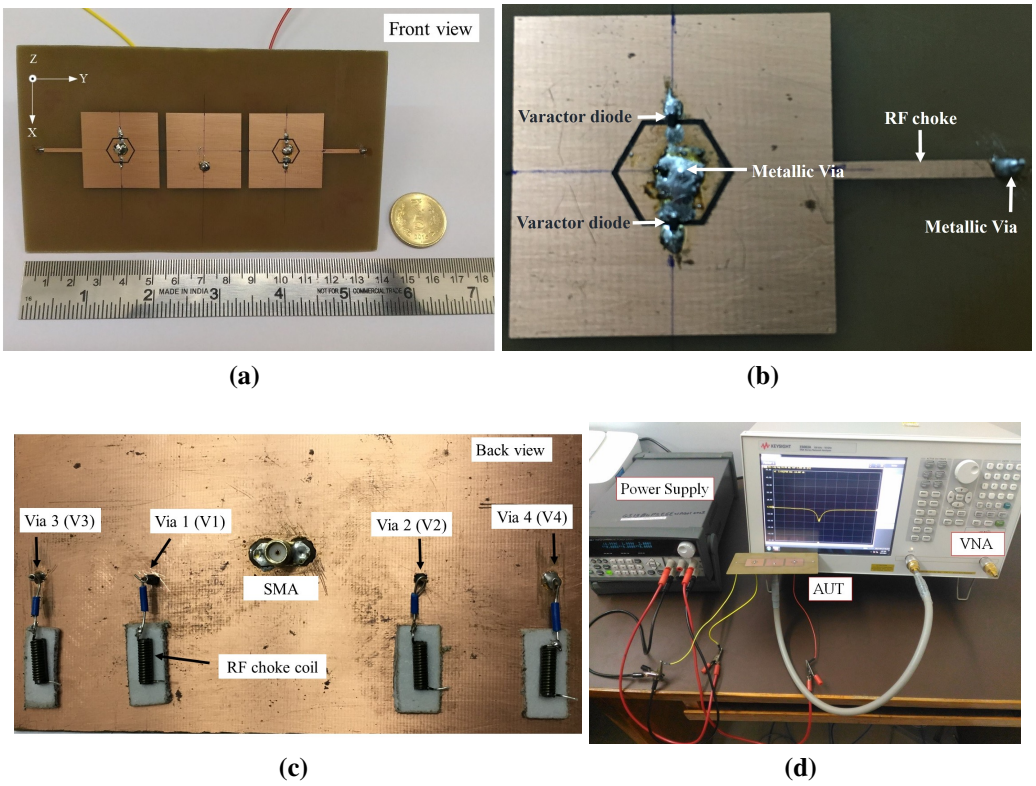

Figure 3.21. Photographs of the fabricated antenna (a) Front view, (b) Magnified view of the tunable parasitic element, (c) Back view and (d) Testing of the antenna on VNA.

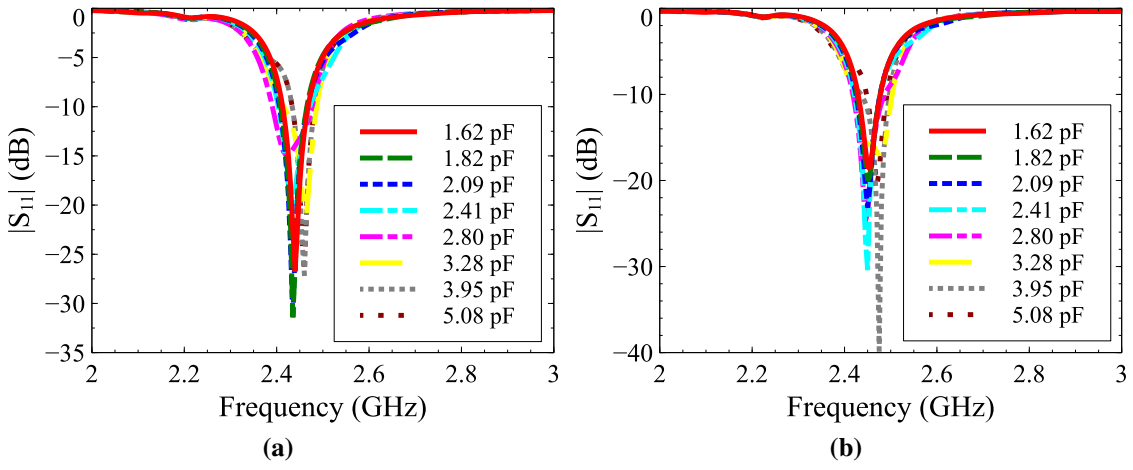

Figure 3.22. Reflection characteristics of the antenna in RD mode (a) Simulated and (b) Measured.

Radiation characteristics of the antenna are tested in a far-field anechoic chamber, as shown in Figure 3.23. The main beam is continuously scanned from 14.4° to 40° in the H-plane, as capacitance is increased from 1.62 to 5.08 pF. Mutual coupling between the driven patch and tunable parasitic element P2 is very weak at 1.82 and 2.09 pF. However, due to strong reflections from the tunable parasitic element P1, the beam is steered to 14.4° and 18°, respectively. For the capacitance range 2.41 to 5.08 pF, P2 shows director behavior, and the beam is scanned from 21.6° and 40°. Figure 3.24 presents a normalized simulated and measured far-field radiation pattern for the capacitance values from 1.62 to 5.08 pF. The main beam is continuously scanned in the H-plane, while the antenna produces a broadside radiation pattern in the E-plane for all the capacitance values. The measured overall 3-dB beamwidth in the RD mode is from $-46.8°$ to 72°. For the higher capacitance values, the radiated beam becomes more directional and due to which the beamwidth decreases. This is the typical behavior of the Yagi antenna in which a large number of directors are used to achieve a highly directional beam. Gain of the antenna is measured using the gain comparison method and is in the range of 0.20 to 2.79 dBi. The difference in simulated and measured gain is mainly due to tolerance in the capacitance value of varactor diode and losses in the biasing wires. Radiation efficiency of the antenna is calculated using measured gain and simulated directivity as $\eta = G_{mes}/D_{sim}$ [34]. Radiation efficiency of the antenna is in the range of 19% to 34%. Overall measured cross-polarization level in this mode is less than -18.04 dB. Table 3.7 summarizes detailed simulated and measured results.

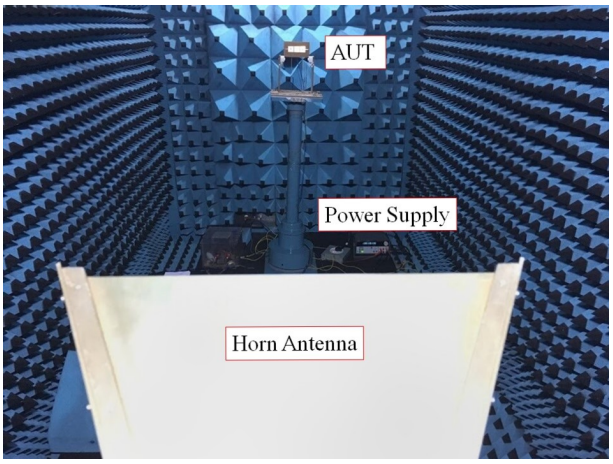

Figure 3.23. Testing setup used in the anechoic chamber to measure radiation characteristics of the fabricated antenna.

3.3.2 Low Radiation Efficiency Issues

It is well known that the lossy nature of the FR4 substrate causes lower gain and reduced radiation efficiency. Factors affecting the radiation efficiency of the proposed antenna are studied, and

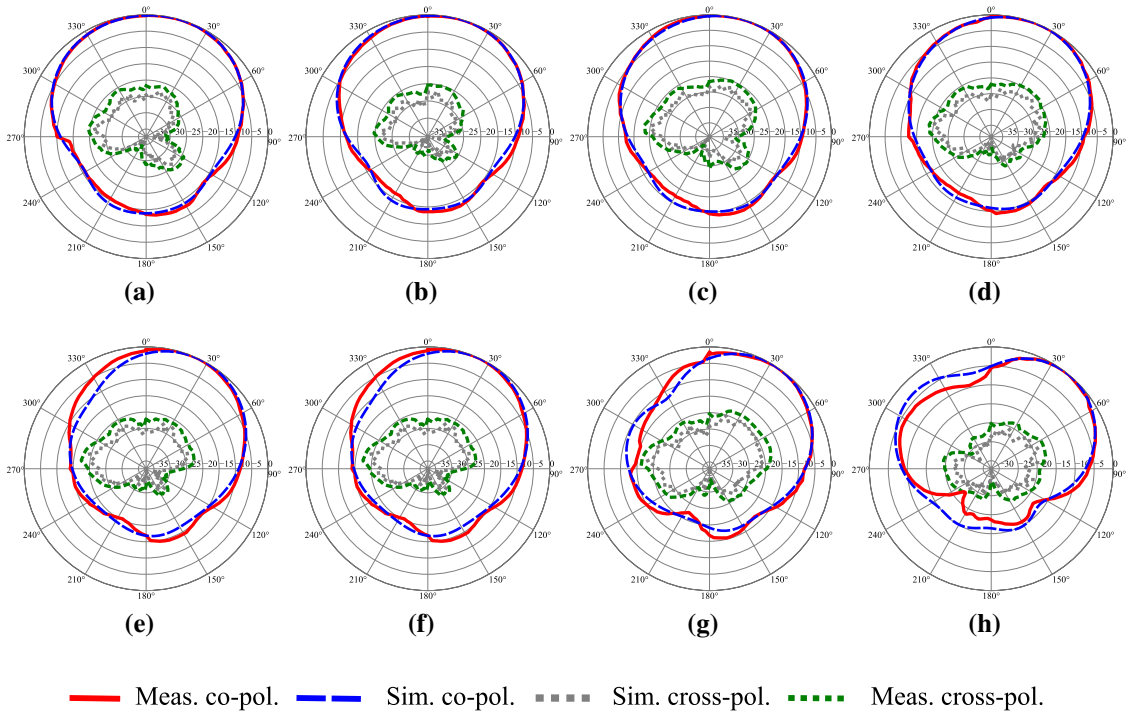

Figure 3.24. Normalized simulated and measured far-field radiation pattern in $\phi = 90°$ plane (RD mode) at 2.45 GHz for capacitance (a) 1.62 pF, (b) 1.82 pF, (c) 2.09 pF, (d) 2.41 pF, (e) 2.8 pF (f) 3.28 pF, (g) 3.95 pF and (h) 5.08 pF.

Table 3.7. Simulated and measured results in the RD Mode.

Capacitance (pF)	Voltage (V)	θ (degree)		3-dB beamwidth (degree)		Gain (dBi)		Cross-polar. ($<$ dB)
		Sim.	Meas.	Sim.	Meas.	Sim.	Meas.	Meas.
1.62	3.5	14.4	14.4	−46.8 to 54 (100.8)	−46.8 to 54 (100.8)	2.19	1.61	−21.53
1.82	3	14.4	14.4	−43.2 to 54 (97.2)	−39.6 to 54 (93.6)	2.52	1.96	−20.24
2.09	2.5	18	18	−32.4 to 54 (86.4)	−36 to 54 (90)	3.06	2.20	−20.38
2.41	2	21.6	21.6	−21.6 to 57.6 (79.2)	−21.6 to 61.2 (82.8)	3.31	2.79	−20.72
2.8	1.5	25.2	25.2	−7.2 to 61.2 (68.4)	−18 to 57.6 (75.6)	3.00	2.50	−21.42
3.28	1	32.4	32.4	0 to 64.8 (64.8)	0 to 64.8 (64.8)	2.11	1.79	−18.04
3.95	0.5	36	36	7.2 to 68.4 (61.2)	10.8 to 68.4 (58.4)	1.08	0.96	−18.28
5.08	0	40	40	10.8 to 72 (61.2)	10.8 to 72 (61.2)	0.24	0.20	−19.05

the results are described in this section. Initially, a square-shaped microstrip patch antenna is simulated in HFSS using FR4 substrate with ϵ_r = 4.3, $\tan\delta$ = 0.02 and h = 1.6 mm. The square-shaped patch achieves 48% radiation efficiency. Then, the antenna is simulated with a driven element and one conventional square-shaped parasitic element placed in the H-plane at 3 mm spacing. The size of both the driven patch and parasitic element is 28.9 mm. The simulation result shows that the the main beam of antenna is scanned to 28° with the radiation efficiency of 24%. Thus, it can be concluded that increased mutual coupling between the antenna elements affects radiation efficiency. Finally, the antenna design is simulated with a square-shaped driven element and one tunable parasitic element placed in the H-plane at a distance of 3 mm. Capacitance of the varactor diodes is varied from 0.84 to 5.08 pF. Radiation efficiency of the antenna is found to be in the range of 23% to 44%. The maximum radiation efficiency is obtained at 1.82 pF capacitance, for which the main beam is radiated in broadside direction. Minimum radiation efficiency is obtained at 5.08 pF when the main beam is steered to 28°. It is found that the gain and radiation efficiency of the antenna is degraded at higher capacitance values. The reason for this degradation is increased I^2R losses, as strong currents are induced on the parasitic elements at higher capacitance values [154]. It can be concluded that factors affecting antenna radiation efficiency are lossy FR4 substrate, mutual coupling, and ohmic losses of the varactor diodes. Radiation efficiency of the antenna can be significantly improved by using low loss microwave substrate and high-quality varactor diodes.

3.3.3 Broadside Mode

The antenna is operated in broadside mode, by keeping P1 and P2 capacitances at 1.82 pF. This capacitance is selected after observing the mutual coupling strength between the driven and parasitic elements P1 and P2. It is found that for 1.82 pF capacitance the coupling between antenna elements is minimum, since both the resonant frequencies f_1 = 2.10 GHz and f_2 = 2.72 GHz are not close to driven element center frequency f. Thus the antenna radiates in broadside direction as the driven element dominates the overall radiation. Measured bandwidth in the broadside mode is from 2.41 to 2.47 GHz. Figure 3.25 displays the simulated and measured reflection characteristics. Normalized radiation pattern plotted in Figure 3.26 shows that the main beam is steered to 0° with the 3-dB coverage from $-39.6°$ to 46.8°. The measured gain and radiation efficiency in this mode is 3.36 dBi and 41%, respectively. Table 3.8 shows the detailed simulated and measured results.

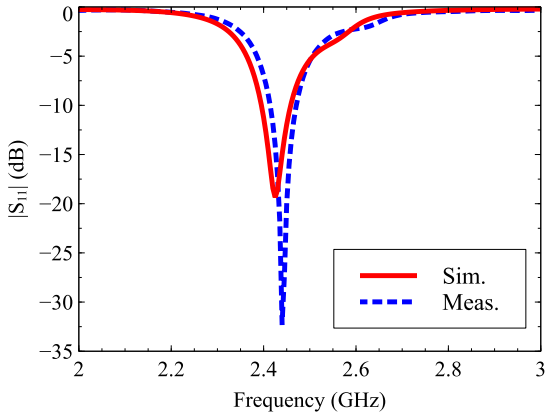

Figure 3.25. Simulated and measured reflection characteristics in the broadside mode.

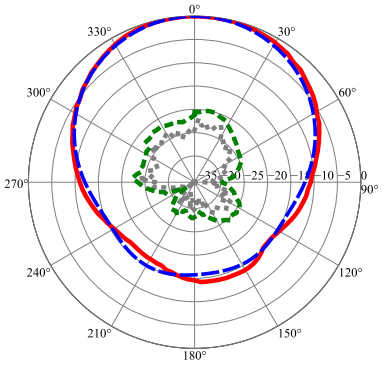

Figure 3.26. Normalized simulated and measured far-field radiation pattern in ϕ = 90° plane (broadside mode) at 2.45 GHz.

Table 3.8. Simulated and measured results in the broadside mode.

Capacitance (pF)	Voltage (V)	θ (degree)		3-dB beamwidth (degree)		Gain (dBi)		Cross-polar. (< dB)
		Sim.	Meas.	Sim.	Meas.	Sim.	Meas.	Meas.
1.82	3	0	0	−39.6 to 39.6 (79.2)	−39.6 to 46.8 (86.4)	3.79	3.36	−20.54

3.3.4 Director-Reflector (DR) Mode

Performance in the DR mode is quite similar to RD mode, with the main beam deflected in $-\theta$ direction. In this mode, the P1 capacitance is varied from 1.62 to 5.08 pF. The reverse voltage applied on the varactor diodes is varied from 3.5 to 0 V. The P2 capacitance is fixed at 0.84 pF by applying a reverse voltage of 15 V. The antenna maintains common impedance bandwidth from 2.43 to 2.48 GHz for all the capacitance values, as shown in Figure 3.27. The main beam in the DR mode is continuously scanned from −14.4° to −40°, as shown in Figure 3.28. It is observed

that the measured 3-dB beamwidth in the DR mode is from −72° to 46.8°. Measured peak gain is in the range of 0.05 to 2.69 dBi. Radiation efficiency of the antenna varies from 19% to 34%. Measured cross-polarization level in the steered direction is found to be less than −17.20 dB. Table 3.9 summarizes the detailed results of the antenna in DR mode.

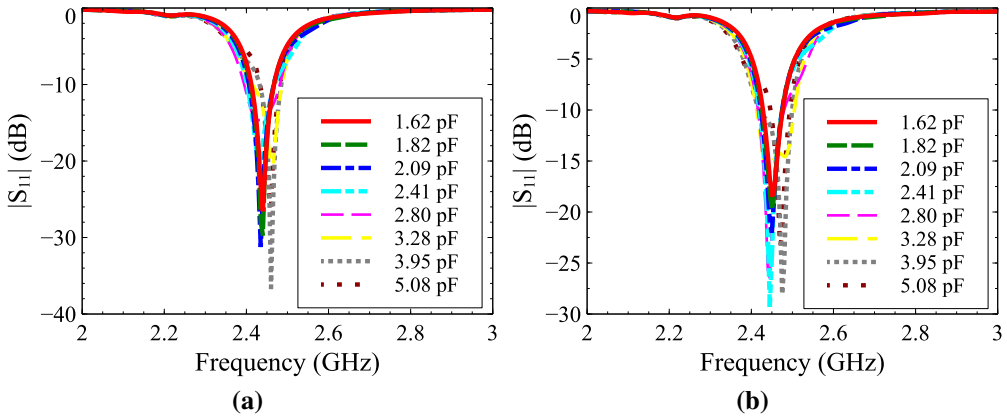

Figure 3.27. Reflection characteristics of the antenna in DR mode (a) Simulated and (b) Measured.

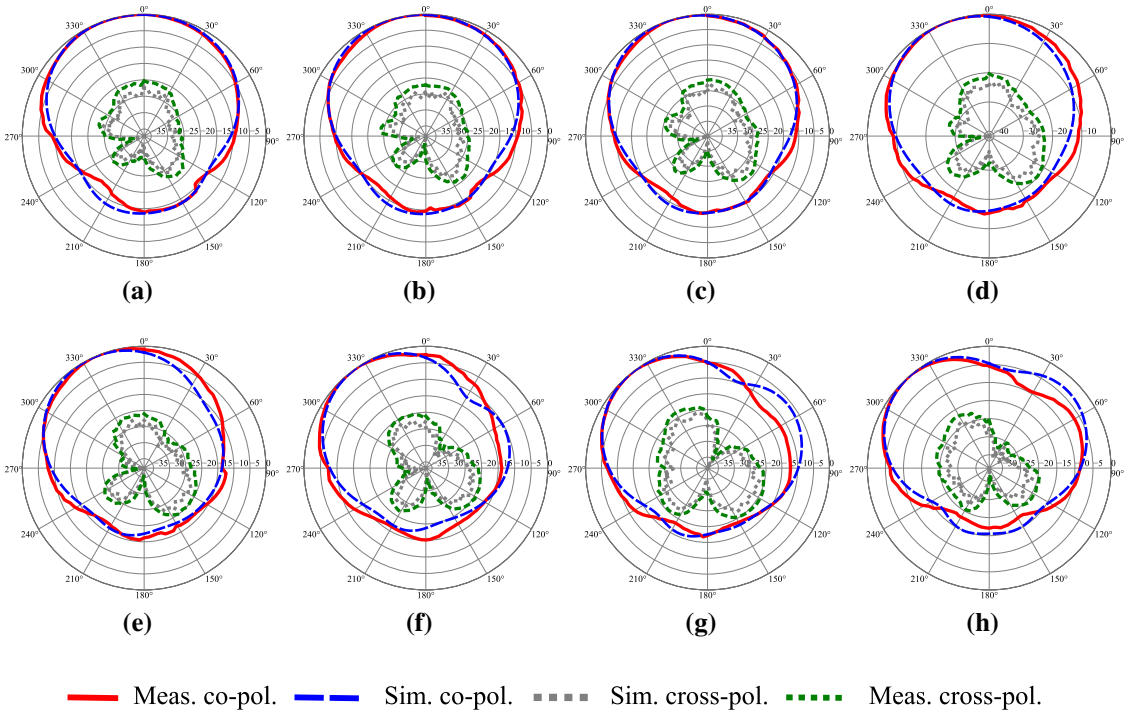

Figure 3.28. Normalized simulated and measured far-field radiation pattern in $\phi = 90°$ plane (DR mode) at 2.45 GHz for capacitance (a) 1.62 pF, (b) 1.82 pF, (c) 2.09 pF, (d) 2.41 pF, (e) 2.8 pF (f) 3.28 pF, (g) 3.95 pF and (h) 5.08 pF.

Table 3.9. Simulated and measured results in the DR Mode.

Capacitance (pF)	Voltage (V)	θ (degree)		3-dB beamwidth (degree)		Gain (dBi)		Cross-polar. ($<$ dB)
		Sim.	Meas.	Sim.	Meas.	Sim.	Meas.	Meas.
1.62	3.5	-14.4	-14.4	-57.6 to 50.4 (108)	-57.6 to 46.8 (104.4)	2.07	1.54	-21.23
1.82	3	-14.4	-14.4	-57.6 to 43.2 (100.8)	-54 to 46.8 (100.8)	2.46	2.02	-22.28
2.09	2.5	-18	-18	-57.6 to 32.4 (90)	-54 to 32.4 (86.4)	2.98	2.30	-22.56
2.41	2	-21.6	-21.6	-57.6 to 21.6 (79.2)	-61.2 to 32.4 (93.6)	3.38	2.46	-22.07
2.8	1.5	-25.2	-25.2	-61.2 to 7.2 (68.4)	-61.2 to 21.6 (82.8)	2.95	2.69	-21.25
3.28	1	-32.4	-32.4	-68.4 to -3.6 (64.8)	-72 to 6 (78)	2.04	1.84	-20.16
3.95	0.5	-36	-36	-68.4 to -7.2 (61.2)	-68.4 to -10.8 (57.6)	0.87	0.67	-18.72
5.08	0	-40	-40	-72 to -7.2 (64.8)	-72 to -14.4 (57.6)	0.10	0.05	-17.20

3.3.5 Performance Comparison

Performance of the proposed PRA is compared with the other reported parasitic antenna designs in terms of the number of parasitic elements, operating bandwidth, beam steering capabilities, peak gain, number of active components used, and type of beam steering. From Table 3.10, it can be seen that the proposed antenna design overcome drawback of discrete beam switching in [6, 47–49] and limited beam scanning in [44, 50–52, 55–57]. In [48], the ground plane truncation method has been used to achieve increased beam scanning up to 50°. However, SLL obtained at the large beam steering angles is very high. Owing to the use of capacitors in [50–52], real-time beam scanning is not possible. The antenna design presented in [44] achieves asymmetrical beam scanning with high SLL, since the performance is experimentally verified with one tunable parasitic element. The ESPAR antenna designs presented in [55, 56] needs additional varactor diodes to maintain the impedance characteristics. Peak gain of the proposed PRA can be improved by using low loss substrate, and it will be comparable to the other reported antenna designs.

Table 3.10. Performance comparison of the proposed 1-D continuous beam scanning PRA with the reported parasitic antenna designs.

Reference	Number of parasitic elements	− 10 dB bandwidth (%)	Main beam elevation plane (degree)	Peak gain (dBi)	Substrate	Switches (number)	Steering type
[6]	2	5.18	−35, 0, 35	n/a	n/a	copper strips (4)	discrete
[47]	2	2.79	−30, 0, 30	6.5	Taconic	PIN (2)	discrete
[48]	4	4.2	−50, −30, 0, 30, 50	7.5	Taconic	PIN (6)	discrete
[49]	4	15	−30, 0, 30	6.5	Rogers	PIN (2)	discrete
[50]	2	1.8	−20 to 20	n/a	Rogers	capacitor (2)	continuous
[51]	2	2.06	−15 to 15	8	Rogers	capacitor (4)	continuous
[52]	2	4.6	−30 to 30	7.5	Rogers	capacitor (2)	continuous
[44]	1	2	−36 to 32	8.1	Rogers	varactor (4)	continuous
[55]	2	n/a	−15 to 15	7.4	Rogers	varactor (8)	continuous
[56]	8	n/a	−20 to 20	12.1	Rogers	varactor (32)	continuous
[57]	4	0.35	−24 to 24	6	Arlon	varactor (2)	continuous
Proposed	2	1.63	−40 to 40	3.36	FR4	varactor (4)	continuous

3.4 Summary

A continuous beam scanning reconfigurable parasitic antenna is designed, simulated, and fabricated. The proposed PRA consists of a probe-feed square-shaped driven element and two tunable parasitic elements placed in the H-plane. The tunable parasitic element shows dual-band behavior, and its performance is analyzed for the capacitance range from 0.84 to 5.08 pF. This antenna works on the principle of microstrip Yagi and tunable parasitic patch size method. Effect of varactor diode capacitance on the mutual coupling between the driven and tunable parasitic elements is studied in detail by calculating the current ratios. Impedance and radiation performance of the antenna is validated in the three operating modes, namely RD, DR, and broadside. The antenna achieves a continuous and improved beam scanning in the H-plane from -40° to 40° with 3-dB coverage from -72° to 72°. Measured common impedance bandwidth of the antenna is from 2.43 to 2.47 GHz. The proposed PRA provides advantages such as simple

and planar structure, improved continuous beam scanning capability, low design complexity, and maintained impedance characteristics in all the operating modes without the requirement of any matching network. The proposed three-element microstrip Yagi antenna design is further extended to form a five-element cross antenna structure to achieve multiple functionalities in a single antenna structure in terms of continuous beam scanning and beamwidth reconfiguration.